AGU PUBLICATIONS

JGR

Journal of Geophysical Research: Space Physics

RESEARCH ARTICLE
10.1002/2017JA023944

Key Points:
- Linear analysis of proton-scale instabilities driven by a tenuous proton ring with large ring speed in relevance to pickup-ion dynamics
- Maximum growth rate of mirror and Bernstein instabilities at oblique propagation is comparable to that of Alfvén-cyclotron instability
- These mirror and Bernstein waves at oblique propagation can aid pitch angle diffusion of pickup ions during the initial growth stage

Correspondence to:
K. Min,
kyungguk.min@jhuapl.edu

Citation:
Min, K., K. Liu, and S. P. Gary (2017), Proton velocity ring-driven instabilities and their dependence on the ring speed: Linear theory, *J. Geophys. Res. Space Physics*, *122*, 7891–7906, doi:10.1002/2017JA023944.

Received 24 JAN 2017
Accepted 24 JUL 2017
Accepted article online 1 AUG 2017
Published online 23 AUG 2017

Proton velocity ring-driven instabilities and their dependence on the ring speed: Linear theory

Kyungguk Min[1], Kaijun Liu[2], and S. Peter Gary[3]

[1]The Johns Hopkins University Applied Physics Laboratory, Laurel, Maryland, USA, [2]Department of Physics, Auburn University, Auburn, Alabama, USA, [3]Space Science Institute, Boulder, Colorado, USA

Abstract Linear dispersion theory is used to study the Alfvén-cyclotron, mirror and ion Bernstein instabilities driven by a tenuous (1%) warm proton ring velocity distribution with a ring speed, v_r, varying between $2v_A$ and $10v_A$, where v_A is the Alfvén speed. Relatively cool background protons and electrons are assumed. The modeled ring velocity distributions are unstable to both the Alfvén-cyclotron and ion Bernstein instabilities whose maximum growth rates are roughly a linear function of the ring speed. The mirror mode, which has real frequency $\omega_r = 0$, becomes the fastest growing mode for sufficiently large v_r/v_A. The mirror and Bernstein instabilities have maximum growth at propagation oblique to the background magnetic field and become more field-aligned with an increasing ring speed. Considering its largest growth rate, the mirror mode, in addition to the Alfvén-cyclotron mode, can cause pitch angle diffusion of the ring protons when the ring speed becomes sufficiently large. Moreover, because the parallel phase speed, $v_{\|ph}$, becomes sufficiently small relative to v_r, the low-frequency Bernstein waves can also aid the pitch angle scattering of the ring protons for large v_r. Potential implications of including these two instabilities at oblique propagation on heliospheric pickup ion dynamics are discussed.

1. Introduction

Space plasmas, including those of the terrestrial and planetary magnetospheres, the solar wind, and the distant boundary regions of the heliosphere, are typically observed to deviate from local thermodynamic equilibrium, exhibiting nonthermal features such as temperature anisotropy and ring/beam velocity distributions. Departures from distributions in thermodynamic equilibrium are a possible source of free energy for many different electromagnetic plasma instabilities, that is, growing modes with both magnetic and electric fluctuations ($\delta\mathbf{B} \neq 0$ and $\delta\mathbf{E} \neq 0$) [e.g., *Gendrin*, 1983; *Gary*, 1993].

Two classic examples of such instabilities are the Alfvén/ion-cyclotron instability and the mirror mode instability driven by proton temperature anisotropies $T_{\perp p}/T_{\|p} > 1$ on bi-Maxwellian proton velocity distributions [e.g., *Gary*, 1992, 1993; *Denton et al.*, 1993; *Shoji et al.*, 2009; *Sulem*, 2011]. (Here and throughout the paper, the subscripts "⊥" and "||" indicate directions perpendicular and parallel to the background magnetic field $\mathbf{B}_0$, respectively.) The former has maximum growth at propagation parallel to $\mathbf{B}_0$ while the latter has maximum growth at propagation oblique to $\mathbf{B}_0$. Both instabilities have wave numbers at $k\lambda_p \lesssim 1$ (where $\lambda_p \equiv c/\omega_{pp}$ is the proton inertial length) and are generally favored by increasing values of $\beta_{\|p} \equiv 8\pi n_p T_{\|p}/B_0^2$ [e.g., *Yoon and Seough*, 2012]. These two instabilities are further distinguished by their real frequencies in that the Alfvén/ion-cyclotron instability satisfies $0 < \omega_r < \Omega_p$ whereas the mirror instability has $\omega_r = 0$. There is an abundant literature on linear theory [e.g., *Davidson and Ogden*, 1975; *Gendrin et al.*, 1984] and computer simulations [e.g., *McKean et al.*, 1992; *Gary et al.*, 1995; *Califano et al.*, 2008; *Shoji et al.*, 2009, 2012; *Herčík et al.*, 2013; *Porazik and Johnson*, 2013; *Riquelme et al.*, 2015; *Hoilijoki et al.*, 2016] of these instabilities, and the electromagnetic fluctuations with characteristics of these instabilities are observed in various space plasmas, including the terrestrial and planetary magnetosheath [e.g., *Denton et al.*, 1993; *Anderson et al.*, 1994; *Gary et al.*, 2001; *André et al.*, 2002; *Hellinger et al.*, 2006; *Volwerk et al.*, 2008; *Dimmock et al.*, 2015], solar wind and heliosheath [e.g., *Tsurutani et al.*, 1992; *Burlaga et al.*, 2006, 2007; *Bale et al.*, 2009], and cometary environments [e.g., *Balsiger et al.*, 1986; *Russell et al.*, 1987; *Gary and Madland*, 1988; *Tsurutani et al.*, 1999]. In addition, the stability condition typically expressed as inverse correlations between $\beta_{\|p}$ and $T_{\perp p}/T_{\|p}$ is reasonably well understood [e.g., *Gary*, 1992; *Denton et al.*, 1993; *Gary and Lee*, 1994; *Kasper et al.*, 2003; *Hellinger et al.*, 2006; *Bale et al.*, 2009; *Yoon and Seough*, 2012].

Other electromagnetic instabilities can be driven by proton velocity distributions that are even more nonthermal than bi-Maxwellians. In particular, the ion Bernstein instability associated with the velocity ring condition $\partial f_p(v_\perp)/\partial v_\perp > 0$ can become unstable at higher frequencies near harmonics of Ω_p and relatively shorter wavelengths $k\lambda_p \gtrsim 1$ [e.g., *Gulelmi et al.*, 1975; *Gary and Madland*, 1988; *Yoon*, 1992; *Boardsen et al.*, 1992; *Dendy et al.*, 1994; *McClements et al.*, 1994; *Horne et al.*, 2000; *Vandas and Hellinger*, 2015]. In Earth's inner magnetosphere, enhanced field fluctuations that peak near harmonics of the proton cyclotron frequency [*Russell et al.*, 1970; *Perraut et al.*, 1982; *Santolík et al.*, 2002; *Walker et al.*, 2016] are frequently observed. Particle measurements associated with these fluctuations show a velocity ring condition in the energetic ion population [*Meredith et al.*, 2008; *Ma et al.*, 2014; *Xiao et al.*, 2013; *Balikhin et al.*, 2015], which can be formed by energy-dependent drift of the injected ring current ions [*Chen et al.*, 2010a, 2010b]. These waves have a strong compressional component of the fluctuating magnetic field and propagate quasi-perpendicular to $\mathbf{B}_0$, consistent with the ion Bernstein modes excited from a tenuous ring population with a ring speed on the order of v_A in a dense cold plasma background [e.g., *Perraut et al.*, 1982; *Boardsen et al.*, 1992; *Horne et al.*, 2000; *Chen et al.*, 2010b]. The waves with proton cyclotron harmonic dispersion are also observed in the plasma sheet boundary layer [*Broughton et al.*, 2008; *Engebretson et al.*, 2010] and Mercury's magnetosphere [*Boardsen et al.*, 2012, 2015], where lack of the cold background in these environments leads to Bernstein waves that are more electromagnetic than those in the inner magnetosphere [*Denton et al.*, 2010; *Gary et al.*, 2010; *Boardsen et al.*, 2015].

Pickup ions in the distant solar wind form perhaps the most extreme nonthermal distribution and are subject to a variety of electromagnetic instabilities. The pickup ions can arise whenever a magnetized plasma flows through a neutral gas [*Zank*, 1999]. The neutrals, e.g., from the local interstellar medium are ionized via charge exchange, photoionization, and/or electron-impact ionization processes, and the newborn ions are subsequently picked up by the solar wind [*Bzowski et al.*, 2008]. The type of the pickup ion velocity distribution function depends on the pickup angle, the angle between the solar wind velocity $\mathbf{v}_{sw}$ and $\mathbf{B}_0$. When $\mathbf{v}_{sw} \cdot \mathbf{B}_0 = 0$, the pickup ions form a ring velocity distribution in the plasma reference frame. But in general, $\mathbf{v}_{sw} \cdot \mathbf{B}_0 \neq 0$. So the pickup ions can possess nonzero bulk motion along $\mathbf{B}_0$ and form a so-called ring-beam distribution, which is also subject to beam-driven instabilities [e.g., *Gary et al.*, 1984]. A typical pickup ion ring speed is quite large ($\sim 10 v_A$), while the thermal spread of the ring is only a fraction of the Alfvén speed [e.g., *Liu et al.*, 2012; *Niemiec et al.*, 2016]. Such (nearly cold) rings can be very unstable even with only a small concentration. There is an abundant literature on linear theory [e.g., *Wu and Davidson*, 1972; *Wu and Hartle*, 1974; *Gary et al.*, 1984; *Gary and Madland*, 1988; *Wu et al.*, 1988; *Summerlin et al.*, 2014] and computer simulations [e.g., *Winske et al.*, 1985; *Winske and Quest*, 1986; *Gary et al.*, 1986; *Florinski et al.*, 2010; *Liu et al.*, 2012; *Florinski et al.*, 2016; *Niemiec et al.*, 2016] of the various kinetic instabilities driven by pickup ions, including the two classic instabilities mentioned earlier.

The motivation of the present study is our recent studies of the ion Bernstein and Alfvén-cyclotron instabilities driven by the ring-like velocity distributions typically found in the terrestrial magnetosphere [*Min and Liu*, 2016a; *Min et al.*, 2016; *Min and Liu*, 2016b, 2016c]. Particularly, *Min and Liu* [2016a], using linear dispersion theory and computer simulations in a magnetized uniform plasma, presented for the first time the two instabilities simultaneously driven by a proton velocity ring distribution with the ring speed and thermal spread on the order of the Alfvén speed. They found that even though the ion Bernstein modes have overall larger linear growth rates than the Alfvén-cyclotron mode, saturation amplitudes can be greater for the Alfvén-cyclotron mode than for the Bernstein modes. This is because the preferential perpendicular velocity scattering of protons by the Bernstein modes leaves the proton temperature anisotropy, $T_{\perp p}/T_{\parallel p}$, relatively unaffected, and thereby the Alfvén-cyclotron mode can grow as predicted by linear theory. In a follow-up paper, *Min et al.* [2016] examined in detail the dependence of the saturation amplitudes of the two instabilities on $T_{\perp p}/T_{\parallel p}$ of the partial shell (another type of distribution function with $\partial f_p(v_\perp)/\partial v_\perp > 0$). It was found that the Alfvén-cyclotron mode can saturate at a larger level than the Bernstein modes even for moderate $T_{\perp p}/T_{\parallel p}$.

We extend the linear analyses in our previous studies to investigate how the Alfvén-cyclotron, mirror mode, and ion Bernstein instabilities driven by a proton ring velocity distribution vary when the proton ring speed becomes large, close to that of the pickup ions in the distant solar wind environment. The general assumptions in the literature have been that magnetospheric ion rings drive unstable only the ion Bernstein modes, whereas solar wind pickup ions preferentially excite only the Alfvén-cyclotron instability. Because the consequences of ion scattering by these instabilities are very different as our previous studies suggested, it is important for understanding ion dynamics in both magnetospheric and solar wind plasmas to critically

examine these assumptions and provide a solid theoretical basis for computer simulations of these modes in such plasmas. Furthermore, it is important to explore potential roles of the ion Bernstein and mirror instabilities on heliospheric pickup ion scattering, whose effects are often neglected in that context.

The paper is organized as follows. Section 2 describes the parameters for the modeled proton velocity distributions, and section 3 presents the full linear dispersion theory results. Section 4 discusses potential implications of including the mirror and Bernstein instabilities at oblique propagation on heliospheric pickup ion scattering, and section 5 provides a summary. We denote jth component's plasma frequency as $\omega_{pj} \equiv \sqrt{4\pi n_j e^2}/m_j$, jth component's cyclotron frequency as $\Omega_j \equiv q_j B_0/m_j c$, jth component's parallel plasma beta as $\beta_{\|j} \equiv 8\pi n_j T_{\|j}/B_0^2$, $\tilde{\beta}_{\|j} \equiv \beta_{\|j} n_0/n_j$ representing dimensionless temperature, the proton inertial length as $\lambda_p \equiv c/\omega_{pp}$ and the Alfvén speed as $v_A \equiv B_0/\sqrt{4\pi n_0 m_p}$. We assume $\mathbf{B}_0 = B_0\mathbf{e}_z$, real wave number $\mathbf{k} = k_\perp \mathbf{e}_x + k_\| \mathbf{e}_z$, and complex wave frequency $\omega = \omega_r + i\gamma$ with $\gamma > 0$ indicating a growing mode.

2. Linear Dispersion Analysis

We adopt the same ring distribution function as in *Min and Liu* [2016a, 2016c], which is given by

$$f_r(v_\|, v_\perp) = \frac{1}{\pi^{3/2}\theta_r^3 A} e^{-v_\|^2/\theta_r^2} e^{-(v_\perp - v_r)^2/\theta_r^2}, \tag{1}$$

where $A = \exp(-v_r^2/\theta_r^2) + \sqrt{\pi}(v_r/\theta_r)\,\mathrm{erfc}\,(-v_r/\theta_r)$ is the normalization constant, v_r and θ_r are the ring speed and the thermal spread of the ring, respectively. Here erfc (x) is the complementary error function. This distribution function was also used in *Summerlin et al.* [2014] and *Florinski et al.* [2016] who were concerned with heliospheric pickup ion stability. The ring velocity distribution of equation (1) is a Gaussian centered around $(v_\|, v_\perp) = (0, v_r)$ in $v_\| - v_\perp$ space. If, for example, the spread in velocities of pickup ions of interstellar origin is negligible, then $\theta_r \approx 0$ and equation (1) becomes a delta function that was used in *Wu and Davidson* [1972] and *Wu et al.* [1988] to derive analytic expressions for growth rate of the Alfvén-cyclotron and mirror instabilities, respectively.

Here we consider a two-component proton distribution where the relatively dense background proton component (denoted with subscript "*c*") is represented by a Maxwellian, and the relatively tenuous and relatively warm proton ring component (denoted with subscript "*r*") is represented by equation (1). In addition, the charge-neutralizing electron population, $n_e = n_c + n_r$, is represented by a Maxwellian (denoted with subscript "*e*"). The realistic proton-to-electron mass ratio and a sufficiently large ratio of $c/v_A = 400$ are used throughout the paper. The parameter c/v_A in the solar wind is much larger, but it has been shown that the three instabilities concerned are not sensitive to c/v_A as long as it is sufficiently large [e.g., *Gary*, 1993; *Gary et al.*, 2012; *Min and Liu*, 2016c; *Fu et al.*, 2016]. In order to examine how the three kinetic instabilities vary with v_r, we construct model distributions with $v_r/v_A = 2, 2.5, 3, 3.5, 4, 5, 6, 7, 8, 9$, and 10. The other parameters are fixed: $\tilde{\beta}_{\|r} = 0.2$ and the relative ring density $n_r/n_e = 0.01$ for the ring component, and $\tilde{\beta}_c = \beta_e = 0.002$ for the background protons and electrons. Note that $\tilde{\beta}_{\|r} = 0.2$ is equivalent to the ring thermal spread $\theta_r \approx 0.45 v_A$. The fixed parameters chosen are more or less consistent with those found in the terrestrial magnetosphere but may differ from the condition found in the region where the heliospheric pickup ions occur. Especially, the background plasma in this region is warmer and the ring component may be more tenuous [e.g., *Florinski et al.*, 2016; *Niemiec et al.*, 2016]. We will briefly consider these situations in section 4 when we discuss implications on heliospheric pickup ion scattering by examining the instability dependence on $\tilde{\beta}_c$ and n_r/n_e for the case of $v_r = 10 v_A$ and for the waves with real frequency $\omega_r \lesssim \Omega_p$.

Given these parameters, the kinetic linear dispersion relation for magnetized, collisionless, uniform plasmas is solved numerically for the complex frequency [*Min and Liu*, 2015]. The dispersion solver used handles the ring distribution of equation (1) directly for any propagation direction. Solutions corresponding to the Alfvén-cyclotron, mirror mode, and ion Bernstein mode instabilities are found in wave number $k \equiv |\mathbf{k}|$ and wave normal angle $\psi \equiv \tan^{-1}(k_\perp/k_\|)$ space. Because we assume a homogeneous, nondrifting plasma in a uniform background magnetic field, we only consider solutions with $\omega_r \geq 0$ for given $k_\| \geq 0$ and $k_\perp \geq 0$.

3. Results

In this section, we focus on the dependence of the three kinetic instabilities on the ring speed of the proton ring distribution in a relatively cool background plasma. Figure 1 shows as an example linear growth rates

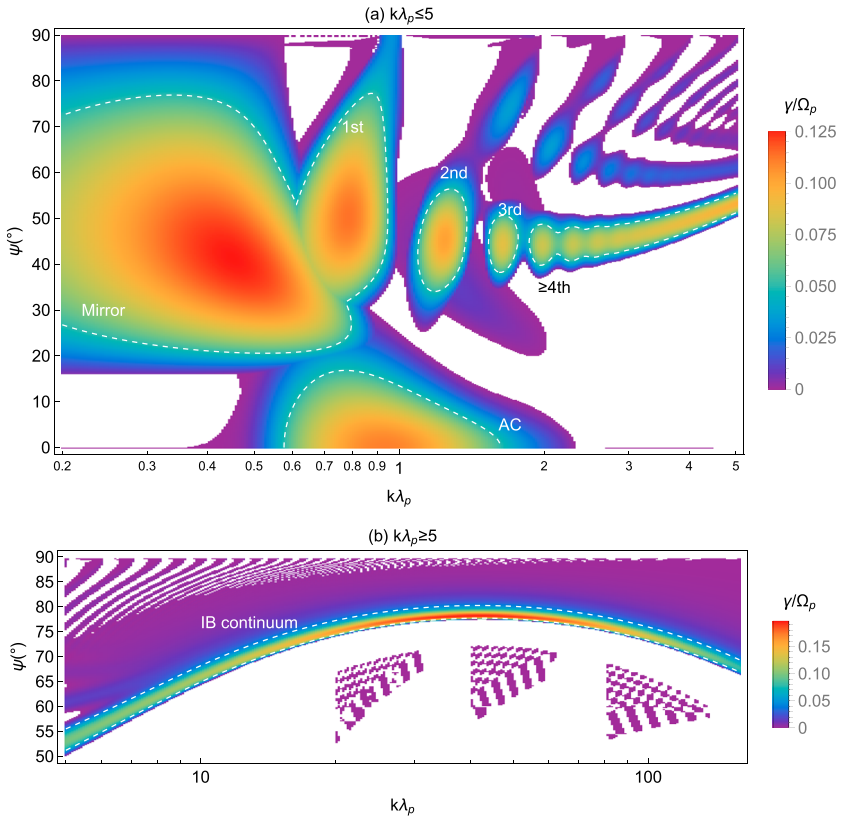

Figure 1. Linear growth rates, $\gamma > 0$, for the $v_r = 5v_A$ case as a function of the wave normal angle, ψ, and wave number, k. (a) The results for the low frequency, long wavelength regime, which contains growing modes of all three kinetic instabilities (as labeled). (b) The results for the high frequency, short wavelength regime where the ion Bernstein modes are the only growing modes. The dashed contours delineate $\gamma = 0.05\Omega_p$. The white area is where the growth rate is negative or where solutions were not found (usually due to severe damping).

(only growing modes) for the $v_r/v_A = 5$ case. Because there can be multiple dispersion surfaces, we chose at each point of (ψ, k) the solution with the maximum growth rate. This ring distribution is unstable to all three types of instabilities that are denoted by the contours and the labels in the figure. As is well known from other studies referenced in section 1, the mirror mode propagates at an oblique angle ($\psi \sim 45°$ for this case) relative to $\mathbf{B}_0$ and has wavelength longer than the proton inertial length ($k\lambda_p < 1$), and the Alfvén-cyclotron mode propagates quasi-parallel to $\mathbf{B}_0$ with $k\lambda_p \sim 1$ [e.g., *Gary*, 1993]. The remaining part of the solutions corresponds to the Bernstein instability. As labeled in the figure, the fundamental mode (labeled "1st") propagates at an oblique angle with $k\lambda_p < 1$ and partially overlaps with the mirror mode. Successive growth rate peaks occur for $1 < k\lambda_p \lesssim 3$ corresponding to higher harmonic Bernstein modes. Beyond $k\lambda_p \sim 3$, the growth rate profile varies smoothly with k in a wide extent of wave number space. The maximum growth rate in the system occurs in this part of the Bernstein instability (Figure 1b) and is slightly larger than that of the mirror mode and Alfvén-cyclotron instabilities. If one considers the growing modes only at $k\lambda_p \lesssim 5$ (Figure 1a), the mirror mode has the largest linear growth rate and is therefore expected to grow fastest during the initial growth phase. There are regions in ψ-k space where the three instabilities overlap, but they are well separated in real frequency space for all values of v_r considered here. Particularly, the mirror mode is nonpropagating, i.e., $\omega_r = 0$, in all cases examined in the present paper. Therefore, in the following subsections, we will examine the properties of these instabilities separately for the chosen values of v_r.

3.1. Alfvén-Cyclotron Mode

The properties of parallel propagating Alfvén-cyclotron mode are well known from other studies referenced in section 1 and analytical formulas derived from simplified linear Vlasov theory [e.g., *Wu and Davidson*, 1972]. Recent studies also make an effort to relate the maximum growth rate and saturation amplitudes with macroplasma parameters for a multispecies plasma [e.g., *Fu et al.*, 2016; *Gary et al.*, 2017]. At propagation parallel to $\mathbf{B}_0$, the detailed structure of the velocity distribution function in the perpendicular velocity direction is

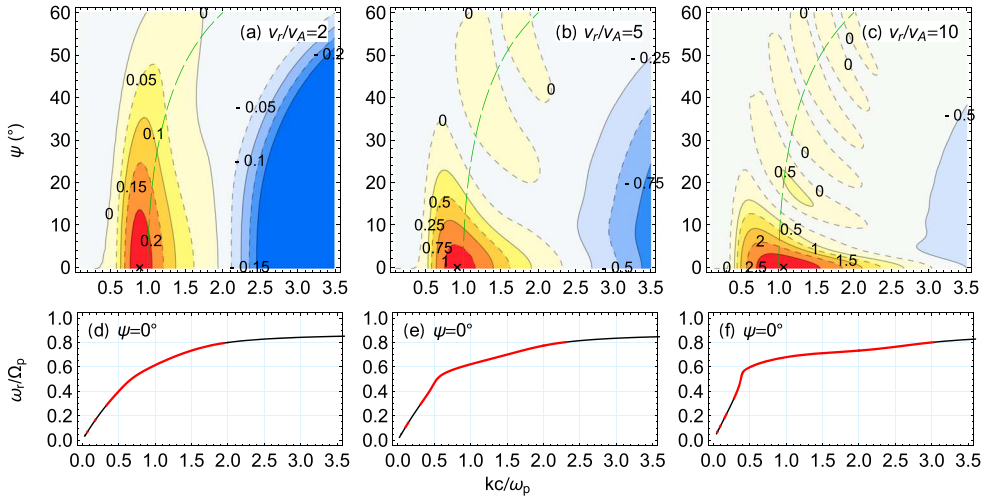

Figure 2. (a–c) Alfvén-cyclotron mode growth rate (γ) contour plots for v_r/v_A = 2, 5, and 10, respectively. The "crosses" mark the location of the largest growth rate. The maximum growth rates are γ_m = 0.0230, 0.111, and 0.291Ω_p, respectively, for v_r/v_A = 2, 5, and 10. The contour labels denote 10γ/Ω_p, and the growing (damping) regions are denoted by warm (cold) color. The long-dashed green curves represent the $k_\parallel \lambda_p = 1$ contour. (d–f) Real frequency as a function of wave number at propagation parallel to $\mathbf{B}_0$ for v_r/v_A = 2, 5, and 10, respectively. The parts with $\gamma > 0$ are highlighted in red. The fixed parameters are $\tilde{\beta}_{\parallel r}$ = 0.2, n_r/n_e = 0.01 and $\tilde{\beta}_c = \beta_e$ = 0.002.

not important as long as the effective perpendicular temperature is the same [e.g., *Brinca and Tsurutani*, 1988], greatly simplifying the linear Vlasov theory. Nevertheless, the relatively weakly growing modes at oblique propagation do depend on the structure of the perpendicular velocity distribution. For this and for completeness, we describe the results from our model plasmas with a particular emphasis on the transition of the instability at oblique propagation.

Figures 2a–2c show growth rate contours of the Alfvén-cyclotron (AC) mode instability for v_r/v_A = 2, 5, and 10, respectively, as a function of ψ and k. Correspondingly, Figures 2d–2f show real frequency versus wave number at propagation parallel to $\mathbf{B}_0$. In all cases, the fastest growing mode denoted by the "x" symbol propagates parallel to $\mathbf{B}_0$, same as the classic bi-Maxwellian-driven AC instability. The most pronounced feature is that with increasing v_r, propagation of the growing mode is confined more to the parallel direction. At the same time, the growing mode occupies a wider k extent. Because the thermal spread of the ring, and thus the parallel temperature, is fixed, the effective perpendicular temperature becomes roughly proportional to v_r^2 for $v_r/\theta_r \gg 1$ (in which case, f_r in equation (1) approaches $\delta(v_\perp - v_r)/2\pi v_r$ and the effective perpendicular temperature of the ring approaches $m_p v_r^2/2$) [e.g., *Wu et al.*, 1988]. The increasing anisotropy leads to an increasing growth rate [e.g., *Gary and Lee*, 1994]. As such, the maximum growth rates are roughly a linear function of v_r (($v_r/v_A, \gamma_m/\Omega_p$) = (2, 0.0230), (2.5, 0.0350), (3, 0.0484), (3.5, 0.0631), (4, 0.0785), (5, 0.111), (6, 0.145), (7, 0.180), (8, 0.216), (9, 0.253), and (10, 0.291) at parallel propagation for all cases). As shown in Figures 2d–2f, the increasing v_r also changes the real frequency of the AC mode as a function of wave number.

Another notable feature is the minor local growth rate peaks at large v_r and at oblique wave normal angles, forming discrete islands of positive wave growth. The locations of these islands appear to follow the constant $k_\parallel$ contour (the green dashed curves denote the $k_\parallel \lambda_p = 1$ contour), which suggests that the resonance condition is involved. Analysis based on a cold background plasma with a cold ring [e.g., *Kennel*, 1966; *Stix*, 1992] suggests that these peaks occur at some multiples of the perpendicular wave number multiplied by the gyroradius of the ring protons. Since the gyroradius of the ring protons increases with their ring speed, more of these minor growth rate peaks arise as v_r becomes large. The decreasing wave normal angle extent of the first peak mentioned earlier can also be explained by this.

3.2. Mirror Mode

Figures 3a–3c show growth rate contours of the mirror instability for v_r/v_A = 3, 5, and 10, respectively, as a function of ψ and k, and Figures 3d–3f show the maximum growth rate (γ_m), the wave normal angle at γ_m and the relative fluctuating magnetic field energy of the fastest growing mode as a function of v_r. With increasing v_r, the propagation direction of the most unstable mirror mode becomes more field-aligned and

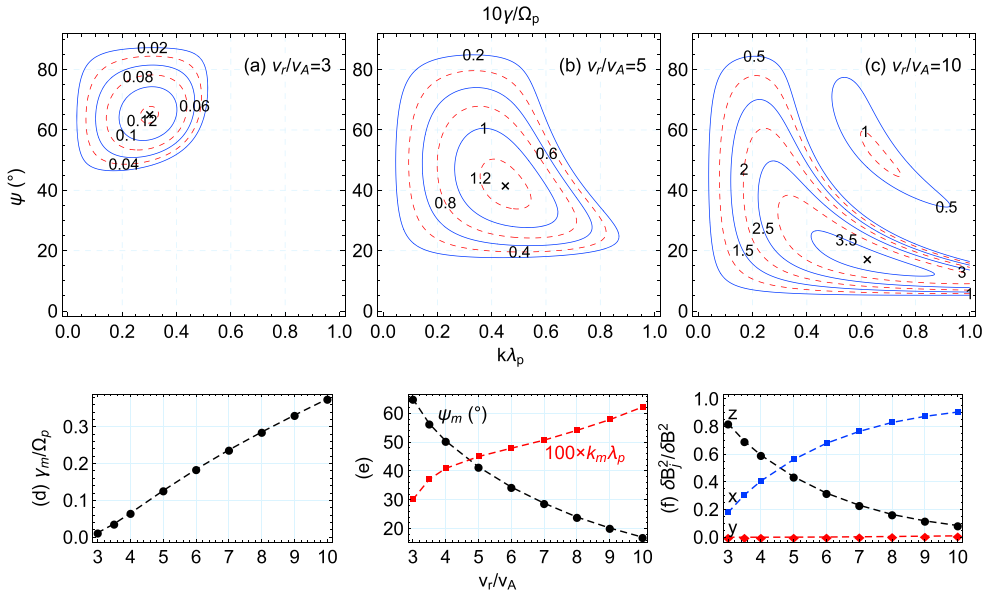

Figure 3. (a–c) Mirror mode growth rate (γ/Ω_p) contours for $v_r/v_A = 3$, 5, and 10. The "crosses" mark the location of the largest growth rate. The contour labels denote $10\gamma/\Omega_p$. (d–f) Properties of the fastest growing mode as a function of v_r: the normalized maximum growth rate γ_m/Ω_p (Figure 3d), the wave normal angle ψ_m and the normalized wave number $k_m\lambda_p$ (multiplied by 100) (Figure 3e), and the relative energy density of the fluctuating magnetic field (Figure 3f). The fixed parameters are $\tilde{\beta}_{\|r} = 0.2$, $n_r/n_e = 0.01$, and $\tilde{\beta}_c = \beta_e = 0.002$. In Figure 3f, the Cartesian components are defined such that wave propagation is contained in the x-z plane and the z direction is parallel to $\mathbf{B}_0$.

the wave length becomes shorter. (The term propagation may not be appropriate for the aperiodic mirror mode, but it should be understood as the wave vector direction.) As for the case of the AC instability, γ_m is roughly a linear function of v_r. The mirror mode excited in a high-beta bi-Maxwellian plasma with temperature anisotropy $T_\perp/T_\| > 1$ is known to have a strong compressional component of the magnetic field fluctuations [e.g., *Hasegawa*, 1969]. In contrast, the present results demonstrate that the ring distributions with sufficiently large v_r can lead to mirror modes with a magnetic compressibility $|\delta B_\||^2/|\delta\mathbf{B}|^2$ much less than unity, despite the small ring density. In Figure 3f, the Cartesian components, x, y, and z, are defined such that $\mathbf{k} \equiv k_\perp\mathbf{e}_x + k_\|\mathbf{e}_z$ with $\mathbf{e}_z = \mathbf{B}_0/B_0$. So the fact that $|\delta B_y|^2/|\delta\mathbf{B}|^2 \ll 1$ for the parameters chosen here means that the propagation direction of the mirror mode is directly related to the compressibility of the fluctuating magnetic field through $\mathbf{k}\cdot\delta\mathbf{B} = 0$: The smaller the wave normal angle is, the smaller the compressibility is. Finally, there also exists a second, relatively weakly growing, mirror mode when $v_r/v_A = 10$. This secondary weakly growing mode is also found for $v_r/v_A = 8$ and 9 (not shown). We surmise that the same mechanism responsible for the minor growth rate peaks of the AC instability (as discussed in the previous paragraph) is operative.

3.3. Ion-Bernstein Mode

This section presents results for the ion Bernstein (IB) instability. Because the IB modes are unstable in a wide k and ω_r domain, we first show the results for $k\lambda_p \le 5$, which approximately corresponds to the low-frequency part of the IB modes. Figures 4a–4c show two-dimensional plots of growth rates and constant real frequency contours for the $v_r/v_A = 2$, 5, and 10 cases, respectively. Because the IB modes can have overlapping dispersion surfaces, these figures, as in Figure 1, only show the solution that yields the maximum growth rate, if there exists multiple solutions at a given point of ψ and k. This is why the real frequency contours in some areas are not smooth. As in the mirror mode case, the readily noticeable features are the more field-aligned propagation direction and the increasing growth rates with increasing v_r. In addition, the lower harmonics are enhanced more quickly such that the fundamental mode becomes the fastest growing mode for $k\lambda_p \le 5$ when $v_r/v_A \gtrsim 5$. The increasing growth rate also appears to result in merging of the two adjacent harmonic modes [e.g., *Chen et al.*, 2016] (above the second harmonic for the $v_r/v_A = 5$ and above the fundamental mode for the $v_r/v_A = 10$ case). To confirm that this is not an artifact of the adapted visualization method, Figures 4d–4i display the real frequency and growth rate versus wave number at a fixed wave normal angle that crosses the maximum growth rate ("x" symbol). Except for the fundamental mode and the $v_r/v_A = 2$ case,

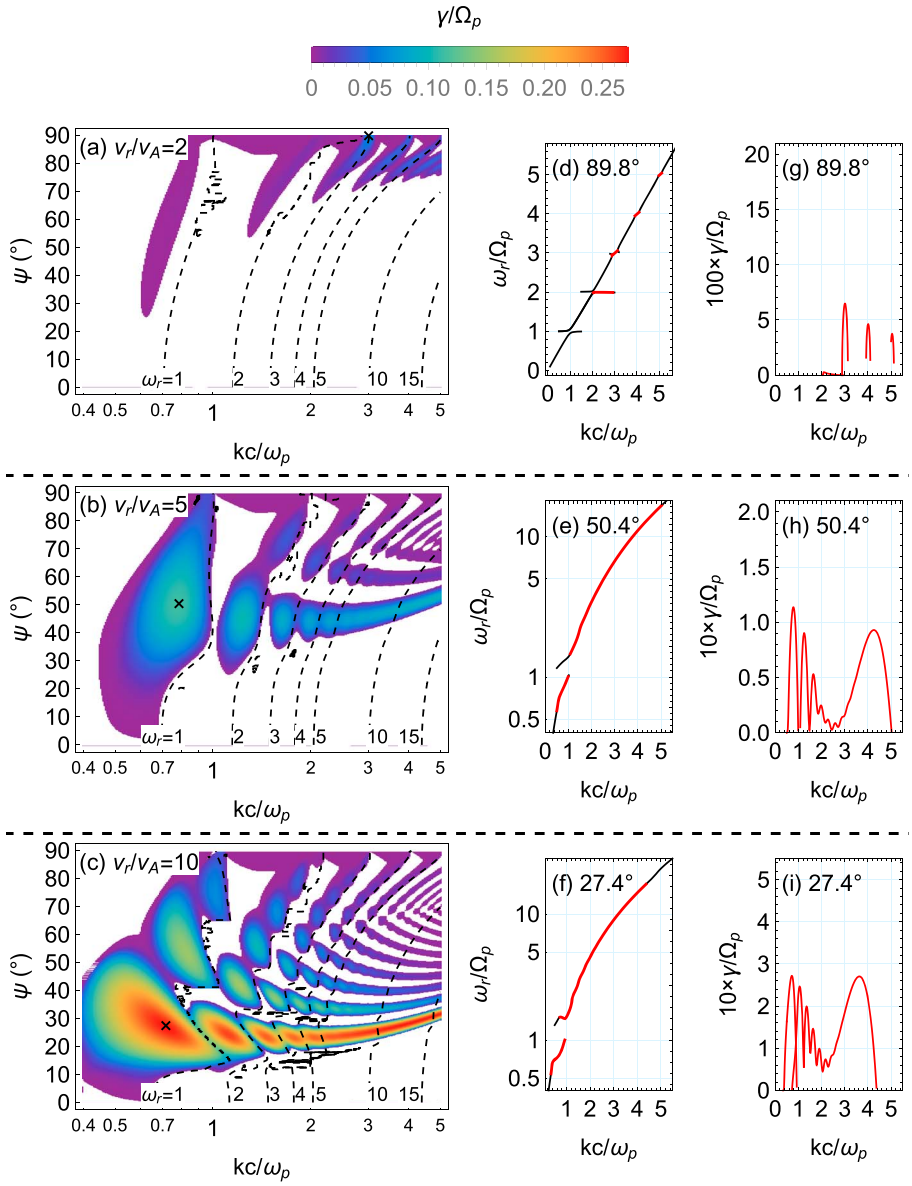

Figure 4. Ion Bernstein instability results: (a–c) Linear growth rates and real frequency contours for $k\lambda_p \leq 5$, roughly corresponding to the low-frequency IB modes. From the top, the figures correspond to the cases for $v_r/v_A = 2$, 5, and 10, respectively. The "crosses" mark the location of the largest growth rate (within the k range plotted). From the top, they are located at $(\psi, k\lambda_p) = (89.8°, 3.01)$, $(50.4°, 0.786)$, and $(27.4°, 0.716)$, respectively, and the corresponding growth rates normalized to Ω_p are 0.0648, 0.114, and 0.272, respectively. The regions where the real frequency contours are disconnected and zigzagged or form islands are due mainly to the discrete nature of the Bernstein mode dispersion relation. (d–f) Real frequency versus wave number at a fixed wave normal angle crossing the "crosses". The parts where the growth rate is positive are highlighted with red. (g–i) Growth rate versus wave number at a fixed wave normal angle crossing the "crosses". Multiplication factors in the vertical scale are different as labeled.

the dispersion curves are continuous and the growth rate is positive over a wide frequency range. Finally, as in the case of the AC instability, there exist successive islands of growing modes that roughly follow constant frequency contours and whose maximum growth rate is a decreasing function of wave normal angle; this is most evidently shown for the $v_r/v_A = 10$ case. The number of these islands increases with the harmonic number as well as v_r.

Figure 5 shows the linear theory properties of the fastest growing Bernstein modes for $\omega_r \leq 5\Omega_p$. Because the maximum growth rates occur below the integer multiples of the proton cyclotron frequency, we choose the maximum at $j - 1 < \omega_r/\Omega_p < j$ for the jth harmonic mode. Similar to the case of the mirror instability shown

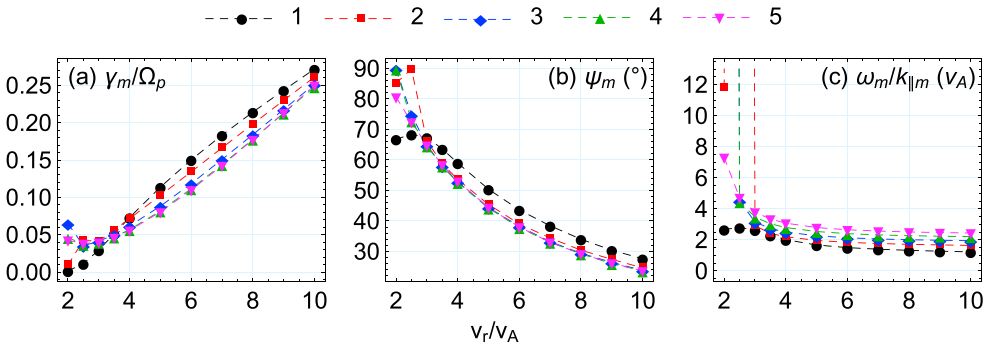

Figure 5. Linear theory properties of the fastest growing Bernstein modes for $\omega_r \leq 5\Omega_p$ as a function of v_r. (The fixed parameters are $\tilde{\beta}_{\|r} = 0.2$, $n_r/n_e = 0.01$, and $\tilde{\beta}_c = \beta_e = 0.002$.) (a) The maximum growth rate, (b) the wave normal angle, and (c) the parallel phase speed ($\omega_m/k_{\|m}$) are plotted as a function of v_r/v_A. The curves of different colors and markers represent the different harmonic modes, as indicated by the legend at the top of the figure.

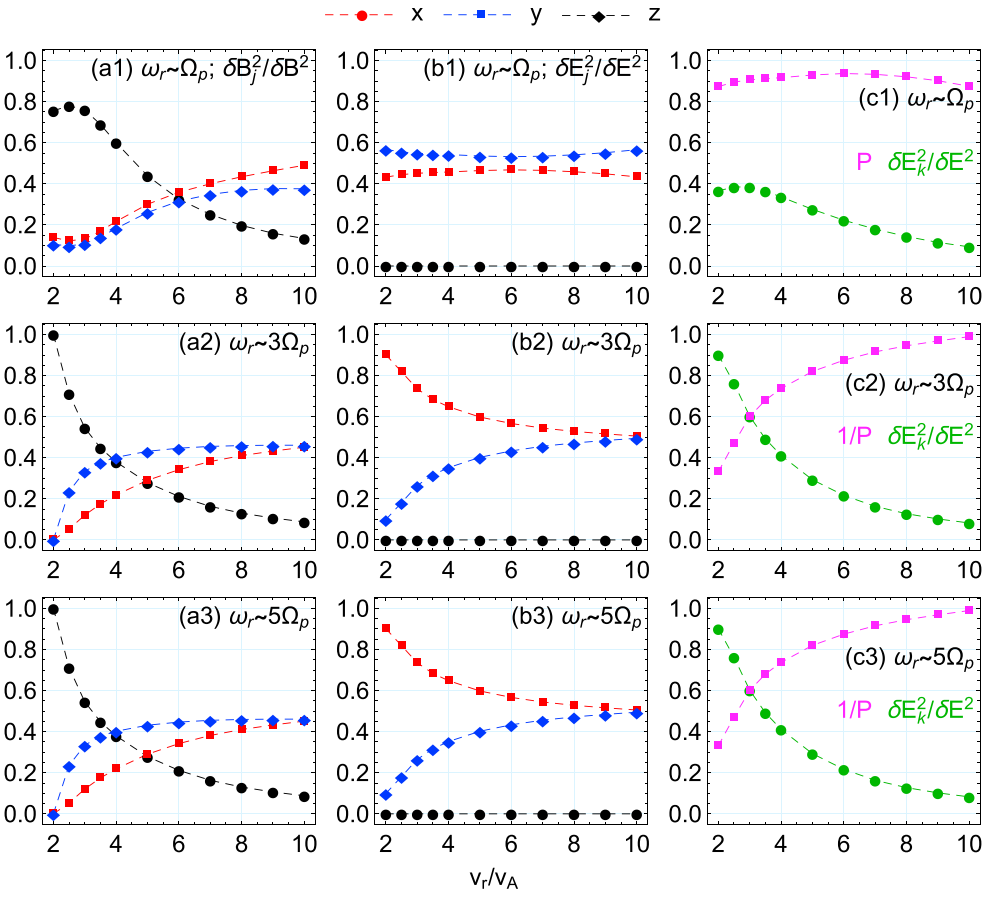

Figure 6. Dimensionless ratios among the fluctuating electric and magnetic field components corresponding to the fundamental (first row), third (second row), and fifth (third row) harmonic modes of the ion Bernstein instability as a function of v_r. Relative amplitudes of the three components of the fluctuating (first column) magnetic and (second column) electric field, and (third column) relative amplitude of the longitudinal component of the fluctuating electric field and the electric field polarization parameter $P = -\delta E_x/\delta E_y$ (Figures 6c2 and 6c3 show $1/P$ while Figure 6c1 shows P). The Cartesian components, x, y, and z, are defined such that $\mathbf{k} \equiv k_\perp \mathbf{e}_x + k_\| \mathbf{e}_z$ with $\mathbf{e}_z = \mathbf{B}_0/B_0$.

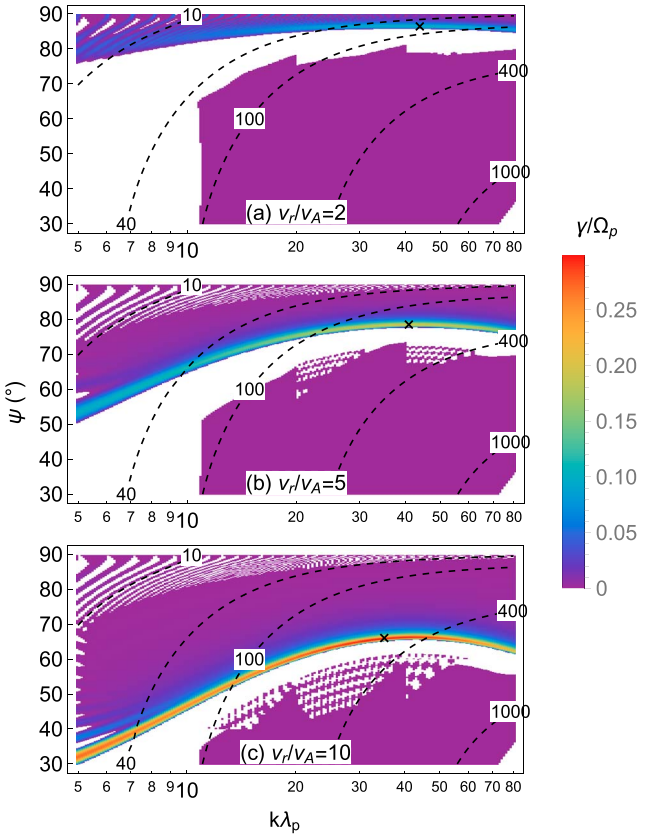

Figure 7. Linear growth rates and real frequencies (in units of Ω_p) corresponding to the high-frequency part of the IB instability for $v_r/v_A = 2$, 5, and 10. The "crosses" mark the location of the largest growth rate (within the ψ and k range plotted).

in Figure 3, the maximum growth rates are almost a linear function of v_r and the wave normal angles are a monotonically decreasing function of v_r. The parallel phase speed $v_{\|ph} \equiv \omega_r/k_\|$ gradually decreases with v_r and remains relatively unchanged at large v_r (Figure 5c). Consequently, $v_r/v_{\|ph}$ is an increasing function of v_r (as will be shown in section 3.4, this ratio mainly determines the diffusion direction of the proton ring distribution at large v_r). Note that due to the near 90° wave normal angles as shown in Figure 5b, the $v_{\|ph}$ values for the third and fourth harmonics at $v_r/v_A = 2$ and the second harmonic at $v_r/v_A = 2.5$ are very large, causing nearly vertical dashed lines in Figure 5c. (Because the upper bound of wave normal angle used in the dispersion solver is 89.8°, $v_{\|ph}/v_A > 100$ for these cases.)

Figure 6 shows some important relative ratios of the fluctuating electric and magnetic fields of the fastest growing fundamental, third harmonic and fifth harmonic modes. The electric field polarization parameter is given by $P = -\delta E_x/\delta E_y$ for $\omega_r > 0$ [*Gary*, 1993]. With increasing v_r, the fastest growing modes become more electromagnetic and more circularly polarized, and the relative amplitude of the compressional component of the magnetic field fluctuations drops quickly. Consequently, the low-frequency Bernstein modes at $v_r/v_A = 10$ have the characteristics of right-handed, nearly circularly polarized waves.

We now move onto the shorter wave length part of the IB instability, which approximately corresponds to the high-frequency part of the IB modes. Figure 7 displays the growth rates and the real frequencies for $v_r/v_A = 2$, 5, and 10. In all cases, the growth rate spectrum is a smooth function of k (or ω_r) except when the propagation direction is quasi-perpendicular to $\mathbf{B}_0$. With increasing v_r, the fastest growing mode moves to smaller wave normal angles and the maximum growth rate increases roughly linearly ($(v_r/v_A, \gamma_m/\Omega_p) =$ (2, 0.0990), (2.5, 0.120), (3, 0.138), (3.5, 0.154), (4, 0.170), (5, 0.197), (6, 0.221), (7, 0.242), (8, 0.262), (9, 0.281), and (10, 0.299)). Unlike the low-frequency counterpart, the fastest growing high-frequency modes remain close

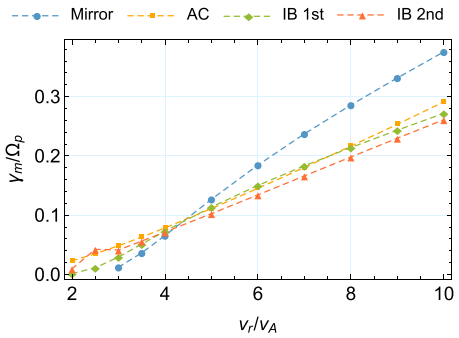

Figure 8. Maximum growth rate γ_m/Ω_p of the three instabilities for real frequency $\omega_r \leq 2\Omega_p$ as a function of ring speed v_r/v_A. The fixed parameters are $\tilde{\beta}_{\|r} = 0.2$, $n_r/n_e = 0.01$, and $\tilde{\beta}_c = \beta_e = 0.002$.

to being electrostatic (with a dominant longitudinal component of the fluctuating electric field) for all v_r values considered.

3.4. Summary of Linear Dispersion Analyses

Figure 8 summarizes the results presented in this section, which shows the maximum growth rate γ_m/Ω_p of the three instabilities for real frequency $\omega_r \leq 2\Omega_p$ as a function of the ring speed. (Figure 5a shows γ_m of the Bernstein instability for $\omega_r \leq 5\Omega_p$.) For the chosen parameters ($\tilde{\beta}_{\|r} = 0.2$, $n_r/n_e = 0.01$ and $\tilde{\beta}_c = \beta_e = 0.002$), γ_m is nearly a linear function of v_r. The Bernstein and Alfvén-cyclotron instabilities have comparable γ_m for all values of v_r. However, the mirror instability has a stronger γ_m dependence on v_r so that its maximum growth rate exceeds that of the other instabilities for $v_r/v_A > 4$. The fact that the mirror mode has the fastest linear growth rate among the three instabilities for larger v_r suggests that the mirror instability will act to reduce the effective temperature anisotropy (by increasing the parallel temperature) of the proton ring distribution [e.g., *Califano et al.*, 2008], potentially slowing down the Alfvén-cyclotron instability growth (more discussion in section 4).

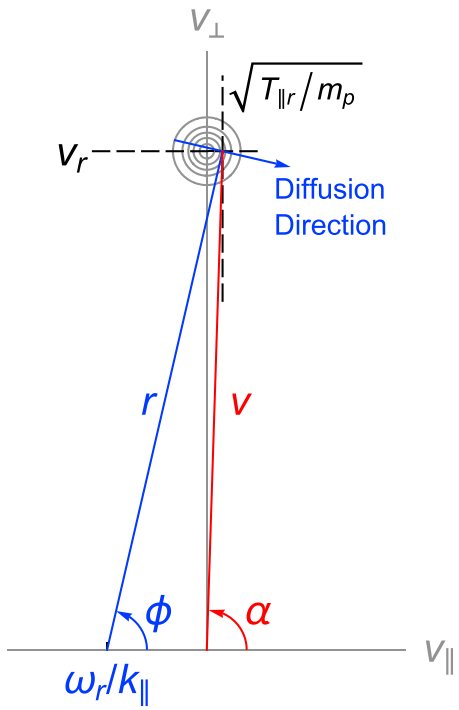

Figure 9. A schematic diagram of quasi-linear diffusion direction of ring protons interacting with the fastest growing low-frequency Bernstein modes shown in Figure 5. The concentric circles depict contours of the ring component phase space density. Considering an interaction between a backward propagating wave with parallel phase speed $v_{\|ph} = |\omega_r/k_\||$ and protons with $v_\| = \sqrt{T_{\|r}/m_p}$ and $v_\perp = v_r$, the symbol definitions are as follows: $v = \sqrt{v_r^2 + T_{\|r}/m_p}$ and $r = \sqrt{v_r^2 + (v_{\|ph} + \sqrt{T_{\|r}/m_p})^2}$, and therefore $\phi = \sin^{-1}(v_r/r)$ and $\alpha = \sin^{-1}(v_r/v)$.

In similar lines, the fastest growing Bernstein mode for large v_r (which has real frequency $\omega_r \approx \Omega_p$) can aid the pitch angle diffusion of the proton ring distribution. According to quasi-linear theory [e.g., *Kennel and Engelmann*, 1966], the increase of $v_r/v_{\|ph}$ shown in Figure 5c (while $\tilde{\beta}_{\|r}$ is fixed) suggests that the pitch angle diffusion by the low-frequency Bernstein modes should be enhanced relative to the energy diffusion for large v_r. To demonstrate this, we estimate the energy and pitch angle diffusion coefficients for large v_r using the schematic diagram of Figure 9 by taking into account only the fastest growing mode. We assume that this wave strongly interacts with the ring protons whose parallel speed is roughly the parallel thermal speed of the ring distribution of equation (1), $|v_\|| \approx \sqrt{T_{\|r}/m_p} = \sqrt{0.1}v_A$ (in fact, the parallel resonant speed is roughly $\sqrt{0.1}v_A$ (not shown)). Then because in quasi-linear theory, the particle energy is conserved in the wave reference frame, diffusion of these particles will occur mainly along (parallel or anti-parallel to) the direction shown in the diagram with a blue arrow, which is tangential to the circle with its center at $v_\| = -|v_{\|ph}|$ (considering interactions with the backward propagating wave) and $v_\perp = 0$ and a radius of $r \equiv \sqrt{v_r^2 + (v_{\|ph} + \sqrt{T_{\|r}/m_p})^2}$. Therefore, the rates at which the parallel and perpendicular speeds change are $dv_\| \propto -\sin\phi d\phi$ and

$dv_\perp \propto \cos\phi d\phi$, respectively, where $\phi = \sin^{-1}(v_r/r)$. Because the rates at which the energy and pitch angle change are $dE \propto d|\mathbf{v}|^2/2 = v_\parallel dv_\parallel + v_\perp dv_\perp$ and $d\alpha \propto (-v_\perp dv_\parallel + v_\parallel dv_\perp)/|\mathbf{v}|^2$ (by differentiating $\cot\alpha = v_\parallel/v_\perp$), respectively, the normalized energy diffusion coefficient and the pitch angle diffusion coefficient are $\tilde{D}_{EE} \equiv D_{EE}/E^2 \propto dE^2/E^2$ and $D_{\alpha\alpha} \propto d\alpha^2$, respectively [e.g., *Liu et al.*, 2010]. Therefore, the ratio of the two coefficients is $\tilde{D}_{EE}/D_{\alpha\alpha} = 4\tan^2(\phi-\alpha) \approx 4(v_{\parallel ph}/v_r)^2$. For $v_r/v_A = 10$, the ratios of the two diffusion coefficients for $v_{\parallel ph}/v_A = 1.5$, 2 and 2.5 are $\tilde{D}_{EE}/D_{\alpha\alpha} = 0.0879$, 0.155 and 0.242, respectively (roughly corresponding to the first, third, and fifth harmonics, respectively; see Figure 5c). In comparison for $v_r/v_A = 4$, the ratios for $v_{\parallel ph}/v_A = 2$, 2.5 and 3 are 0.842, 1.27, and 1.78, respectively (roughly corresponding to the first, third, and fifth harmonics, respectively). With fixed $v_{\parallel ph}/v_A = 3$, $\tilde{D}_{EE}/D_{\alpha\alpha} < 1$ for $v_r/v_A > 5$, so the pitch angle diffusion by the Bernstein modes with $\omega_r/\Omega_p \lesssim 5$ becomes appreciable for $v_r/v_A \gtrsim 6$.

4. Implications on Heliospheric Pickup Ion Scattering

The results obtained here may have potential implications on the pickup ion dynamics [*Wu et al.*, 1986], an integral component of the secondary energetic neutral atom (ENA) mechanism [*Heerikhuisen et al.*, 2010]. The most startling result of the Interstellar Boundary EXplorer (IBEX) mission, a single satellite mission with the objective of discovering the global interaction between the solar wind and the interstellar medium [*McComas et al.*, 2005, 2009a], has been the discovery of an annular bright ribbon of ENA emission with a threefold enhancement near 1 keV [*McComas et al.*, 2011, 2014], because this ribbon was not predicted by any pre-IBEX theories or models [e.g., *McComas et al.*, 2009b; *Schwadron et al.*, 2009]. The so-called secondary ENA mechanism was elaborated by *Heerikhuisen et al.* [2010] who successfully reproduced the main features of the ribbon. The main challenge has since been quantifying the previously omitted stage of the pickup ion velocity distribution evolution between two consecutive occurrences of the charge exchange in the outer heliosheath [*Gamayunov et al.*, 2010; *Möbius et al.*, 2013]. The evolution consists of three stages [e.g., *Wu et al.*, 1986]: (1) formation of the ring-beam, (2) isotropization by self-generated fluctuations to produce a shell, and (3) thermalization of the shell by, e.g., broadband turbulence. The secondary ENA mechanism relies on a very important assumption that the pickup ions should not diffuse significantly before charge exchange can convert them into secondary ENAs, some of which travel to the inner heliosphere where they can be observed by IBEX [*Heerikhuisen et al.*, 2010]. However, because the pickup ion velocity distributions that were assumed to be a narrow ring are inherently very unstable, whether they can be sustained long enough to produce the observed ENA flux levels in the ribbon before being pitch angle scattered has been under debate [*Florinski et al.*, 2010; *Gamayunov et al.*, 2010].

Several studies have considered more realistic parameters for the pickup ion velocity distribution in an attempt to remedy this problem. *Liu et al.* [2012] carried out a series of one-dimensional hybrid simulations involving the pickup ions continuously injected into the system. Although the more realistic, slow buildup of pickup ions in the system was able to alleviate the pitch angle scattering time scale in the outer heliosheath, it is still considerably shorter than the minimum scattering time scale of years required by the secondary ENA mechanism. A simple solution to this scattering problem has been proposed by *Summerlin et al.* [2014]. *Summerlin et al.* [2014] showed that growth rates are highly sensitive to the parallel temperature of the ring distribution, $T_{\parallel r}$, and even modest $T_{\parallel r}$ are sufficient to damp the parallel propagating self-generated waves. *Florinski et al.* [2016] extended the study of *Summerlin et al.* [2014] and found, for a 90° pickup angle, a gap in $T_{\parallel r}$ space where the parallel propagating mode is stable. This stability gap was subsequently confirmed with one-dimensional hybrid simulations. This is a consequence of a competition between wave growth by the ring and damping by the warm Maxwellian core. The ring mode (with real frequency $\omega_r \approx \Omega_p$ examined by *Summerlin et al.* [2014]) and the Alfvén-cyclotron mode (with $\omega_r < \Omega_p$) become unstable for the ring distribution with cooler and warmer ring temperature, respectively. They found that in general a ring distribution whose parallel thermal spread exceeds the thermal spread of the core plasma would be unstable and diffuse toward isotropy. If the initial ring distribution falls in this stability gap, it can be sustained long enough to have the charge exchange necessary to make up the ribbon ENA fluxes.

The results in section 3 suggest that the stability gap argument may not work once the mirror and Bernstein instabilities at oblique propagation are taken into account. Although the ring distribution may be stable to the Alfvén-cyclotron/ring mode instability at quasi-parallel propagation for an intermediate value of $T_{\parallel r}$, it can be unstable to the instabilities at oblique propagation. These oblique modes should aid pitch angle diffusion of the initial ring distribution (at least during the initial growth phase). Especially, the mirror mode has the

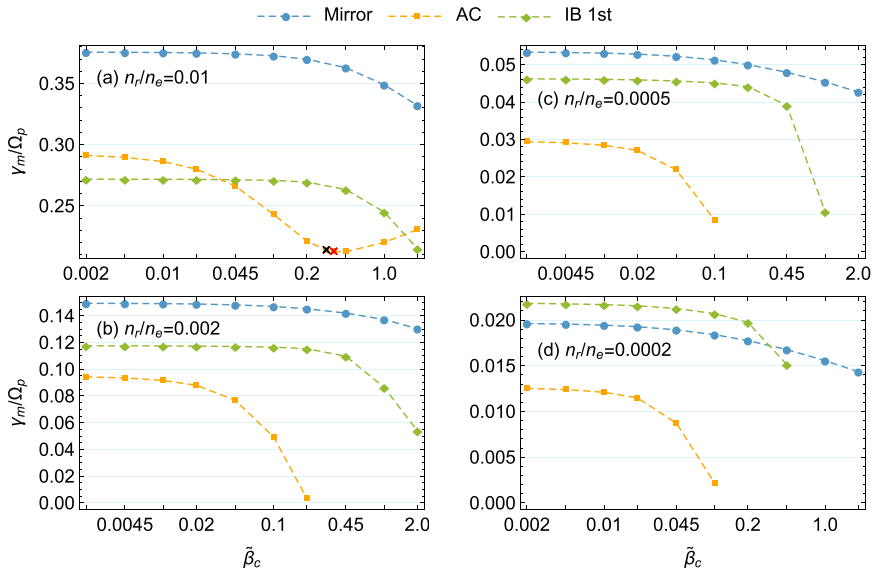

Figure 10. Maximum growth rates of the mirror, Alfvén-cyclotron, and Bernstein (only the fundamental mode) instabilities for $\tilde{\beta}_c$ = 0.002, 0.0045, 0.01, 0.02, 0.045, 0.1, 0.2, 0.45, 1, and 2 and n_r/n_e labeled in the figure. Additionally for $n_r/n_e = 0.01$, the maximum growth rates of the Alfvén-cyclotron instability for $\tilde{\beta}_c = 0.3$ and 0.35 are denoted by the black and red crosses, respectively. The other parameters are $\tilde{\beta}_{\|r} = 0.2$, $v_r/v_A = 10$, $c/v_A = 400$, and $\beta_e = \tilde{\beta}_c$.

largest growth rate for large values of the ring speed. Therefore, this mode can grow fastest and has the potential to reduce the free energy for the Alfvén-cyclotron mode growing at a slower rate by scattering the ring protons along the parallel velocity direction through Landau resonance [*Califano et al.*, 2008]. On the other hand, it is likely that the initial ring distribution whose thermal spread falls into the stability gap can later have an increased thermal spread due to the pitch angle diffusion by these oblique waves such that the evolved distribution can now be unstable to the Alfvén-cyclotron instability at parallel propagation.

We should note that some parameters used in section 3 differ from those assumed in the recent pickup ion studies mentioned above. Especially, the core background plasma is hotter than the one used here. (For example, the parameters assumed in *Florinski et al.* [2016] are $c/v_A \approx 1.4 \times 10^3$, $\tilde{\beta}_c = \beta_e \approx 0.77$, $n_r = 10^{-3} n_e$, and $v_r \approx 22 v_A$.) For more appropriate comparison, we examined the instability dependence on $\tilde{\beta}_c$ and n_r. Only the $v_r = 10 v_A$ case and the waves with the real frequency $\omega_r \lesssim \Omega_p$ were considered, and electron beta β_e is set to equal to $\tilde{\beta}_c$. The other parameters fixed are $c/v_A = 400$ and $\tilde{\beta}_{\|r} = 0.2$ (as in section 3).

Figure 10a shows the maximum growth rates of the mirror, Alfvén-cyclotron and Bernstein (only the fundamental mode) instabilities as a function of $\tilde{\beta}_c$ for $n_r/n_e = 0.01$. It is worth noting that the Alfvén-cyclotron mode transitions to the ring mode examined by *Summerlin et al.* [2014] for $\tilde{\beta}_c$ somewhere between 0.3 and 0.35 indicated by the black and red crosses, respectively. For the parameters used, however, the transition is smooth without a stability gap, although there exists a slight depression of the maximum growth rate. In addition, this ring mode at $\psi \lesssim 10°$ is connected to the fundamental Bernstein mode whose growth rate is maximized at $\psi \sim 30°$ (not shown). (When $\beta_c > 0.2$, the dispersion relation is severely distorted.) Interestingly, the maximum growth rates of the oblique modes are comparable or exceed that of the Alfvén-cyclotron mode at least for $\tilde{\beta}_c \lesssim 2$. This result suggests that the waves at oblique propagation can play a substantial role in the pickup ion scattering in this $\tilde{\beta}_c$ regime, especially for an intermediate value of $\tilde{\beta}_{\|r}/\tilde{\beta}_c$ at which the stability gap may exist. Figure 10b shows the results for a more tenuous ring with $n_r/n_e = 0.002$. In this case, the maximum growth rate of the Alfvén-cyclotron mode at parallel propagation decreases more quickly than the other waves at oblique propagation, and the Alfvén-cyclotron mode becomes stable for $\tilde{\beta}_c \gtrsim 0.45$ (the ring mode may be unstable for $\tilde{\beta}_c > 2$). Figures 10c and 10d show the results for even more tenuous rings ($n_r/n_e = 0.0005$ and 0.0002, respectively). As the ring density decreases further, the maximum growth rate of the Alfvén-cyclotron mode decreases faster than the other modes. This trend suggests that the oblique modes can become the dominant agent for the ring proton scattering when the pickup ion ring is tenuous.

5. Summary

In this study, we used kinetic linear dispersion theory to carry out an in-depth analysis of the Alfvén/ion-cyclotron, mirror mode, and ion Bernstein instabilities driven by a warm proton ring velocity distribution with a varying ring speed, in the presence of relatively cool background proton and electron populations. The ring component is warm in that it has a finite thermal spread on the order of the Alfvén speed, v_A, along both the perpendicular and parallel velocities with respect to the background magnetic field, $\mathbf{B}_0$. The ring speed was varied between $2v_A$ and $10v_A$, and the ring density was assumed to be 1% of the plasma density. For these parameters, the maximum growth rates of all three instabilities are nearly a linear function of ring speed. The Bernstein and Alfvén-cyclotron instabilities have comparable maximum growth rates for all values of ring speed, and the mirror instability has the largest growth rate for $v_r/v_A > 4$. Our principal findings can be summarized as follows. (1) The Alfvén-cyclotron instability has the maximum growth rate at propagation parallel to $\mathbf{B}_0$ for all values of v_r/v_A considered. An increasing effective temperature anisotropy due to an increase of v_r/v_A leads to an increase of the maximum growth rate almost linearly with v_r/v_A. The wave normal angle extent of the unstable modes shrinks with increasing v_r/v_A. (2) The ring distribution assumed is nearly mirror mode stable when $v_r = 2v_A$. However, the growth rate increases almost linearly for $v_r > 2v_A$ and becomes the largest among the three instabilities for $v_r = 10v_A$. The fastest growing mirror mode also shifts toward more quasi-parallel propagation (wave normal angle less than 20° when $v_r/v_A = 10$), and its magnetic compressibility $|\delta B_\parallel|^2/|\delta\mathbf{B}|^2$ decreases. (3) Propagation of the low-frequency part of the ion Bernstein instability also becomes more field-aligned at larger v_r/v_A (wave normal angle $\sim$ 30° when $v_r/v_A = 10$). Because the ratio of the ring speed of the ring protons to the parallel phase speed of the Bernstein waves is approximately 5 for $v_r/v_A = 10$ (the cyclotron resonant speed is $\sim 0.3v_A$), the proton scattering by the enhanced low-frequency Bernstein waves is mainly pitch angle diffusion.

Implications of the mirror and Bernstein instabilities at an oblique propagation angle relative to $\mathbf{B}_0$ on the heliospheric pickup ion scattering were discussed. For more appropriate comparison, we examined the instability dependence on the core plasma temperature and the ring density for the case of $v_r/v_A = 10$ and for the waves with $\omega_r \leq \Omega_p$. The results suggest that the oblique waves are expected to have substantial influence on the evolution of the pickup ion ring during the initial stage of the wave development. It is expected that at the initial stage, these waves should aid pitch angle diffusion of the pickup ions and can affect growth of the Alfvén-cyclotron waves by modifying the initial ring distribution. It should be noted that this hypothesis is based on linear theory. Better understanding of the interplay of the three instabilities presented, therefore, requires self-consistent kinetic simulations [e.g., *Niemiec et al.*, 2016] that describe the quasi-linear and nonlinear processes beyond the linear growth stage.

Acknowledgments
Data supporting the figures presented are available upon request from the corresponding author. This work was supported by NASA grant NNX16AM98G.

References

Anderson, B. J., S. A. Fuselier, S. P. Gary, and R. E. Denton (1994), Magnetic spectral signatures in the Earth's magnetosheath and plasma depletion layer, *J. Geophys. Res.*, *99*, 5877–5891, doi:10.1029/93JA02827.

André, N., G. Erdös, and M. Dougherty (2002), Overview of mirror mode fluctuations in the Jovian dusk magnetosheath: Cassini magnetometer observations, *Geophys. Res. Lett.*, *29*, 1980, doi:10.1029/2002GL015187.

Bale, S. D., J. C. Kasper, G. G. Howes, E. Quataert, C. Salem, and D. Sundkvist (2009), Magnetic fluctuation power near proton temperature anisotropy instability thresholds in the solar wind, *Phys. Rev. Lett.*, *103*(21), 211101, doi:10.1103/PhysRevLett.103.211101.

Balikhin, M. A., Y. Y. Shprits, S. N. Walker, L. Chen, N. Cornilleau-Wehrlin, I. Dandouras, O. Santolik, C. Carr, K. H. Yearby, and B. Weiss (2015), Observations of discrete harmonics emerging from equatorial noise, *Nat. Commun.*, *6*, 7703, doi:10.1038/ncomms8703.

Balsiger, H., K. Altwegg, F. Buehler, S. A. Fuselier, J. Geiss, R. Goldstein, A. J. Lazarus, A. Meier, M. Neugebauer, and U. Rettenmund (1986), The composition and dynamics of cometary ions in the outer coma of Halley, in *ESA Proceedings of the 20th ESLAB Symposium on the Exploration of Halley's Comet*, edited by B. Battrick, E. J. Rolfe, and R. Reinhard, pp. 99–103, ESA Spec. Publ., Pasadena, Calif.

Boardsen, S. A., D. L. Gallagher, D. A. Gurnett, W. K. Peterson, and J. L. Green (1992), Funnel-shaped, low-frequency equatorial waves, *J. Geophys. Res.*, *97*, 14,967–14,976, doi:10.1029/92JA00827.

Boardsen, S. A., J. A. Slavin, B. J. Anderson, H. Korth, D. Schriver, and S. C. Solomon (2012), Survey of coherent ~1 Hz waves in Mercury's inner magnetosphere from MESSENGER observations, *J. Geophys. Res.*, *117*, A00M05, doi:10.1029/2012JA017822.

Boardsen, S. A., E.-H. Kim, J. M. Raines, J. A. Slavin, D. J. Gershman, B. J. Anderson, H. Korth, T. Sundberg, D. Schriver, and P. Travnicek (2015), Interpreting ~1 Hz magnetic compressional waves in Mercury's inner magnetosphere in terms of propagating ion-Bernstein waves, *J. Geophys. Res. Space Physics*, *120*, 4213–4228, doi:10.1002/2014JA020910.

Brinca, A. L., and B. T. Tsurutani (1988), Survey of low-frequency electromagnetic waves stimulated by two coexisting newborn ion species, *J. Geophys. Res.*, *93*, 48–58, doi:10.1029/JA093iA01p00048.

Broughton, M. C., M. J. Engebretson, K.-H. Glassmeier, Y. Narita, A. Keiling, K.-H. FornaçOn, G. K. Parks, and H. RèMe (2008), Ultra-low-frequency waves and associated wave vectors observed in the plasma sheet boundary layer by Cluster, *J. Geophys. Res.*, *113*, A12217, doi:10.1029/2008JA013366.

Burlaga, L. F., N. F. Ness, and M. H. Acuna (2006), Trains of magnetic holes and magnetic humps in the heliosheath, *Geophys. Res. Lett.*, *33*, L21106, doi:10.1029/2006GL027276.

Burlaga, L. F., N. F. Ness, and M. H. Acuna (2007), Linear magnetic holes in a unipolar region of the heliosheath observed by Voyager 1, *J. Geophys. Res.*, *112*, A07106, doi:10.1029/2007JA012292.

Bzowski, M., E. Möbius, S. Tarnopolski, V. Izmodenov, and G. Gloeckler (2008), Density of neutral interstellar hydrogen at the termination shock from Ulysses pickup ion observations, *Astron. Astrophys.*, *491*, 7–19, doi:10.1051/0004-6361:20078810.

Califano, F., P. Hellinger, E. Kuznetsov, T. Passot, P. L. Sulem, and P. M. TráVníčEk (2008), Nonlinear mirror mode dynamics: Simulations and modeling, *J. Geophys. Res.*, *113*, A08219, doi:10.1029/2007JA012898.

Chen, L., R. M. Thorne, V. K. Jordanova, C.-P. Wang, M. Gkioulidou, L. Lyons, and R. B. Horne (2010a), Global simulation of EMIC wave excitation during the 21 April 2001 storm from coupled RCM-RAM-HOTRAY modeling, *J. Geophys. Res.*, *115*, A07209, doi:10.1029/2009JA015075.

Chen, L., R. M. Thorne, V. K. Jordanova, and R. B. Horne (2010b), Global simulation of magnetosonic wave instability in the storm time magnetosphere, *J. Geophys. Res.*, *115*, A11222, doi:10.1029/2010JA015707.

Chen, L., J. Sun, Q. Lu, X. Gao, Z. Xia, and Z. Zhima (2016), Generation of magnetosonic waves over a continuous spectrum, *J. Geophys. Res. Space Physics*, *121*, 1137–1147, doi:10.1002/2015JA022089.

Davidson, R. C., and J. M. Ogden (1975), Electromagnetic ion cyclotron instability driven by ion energy anisotropy in high-beta plasmas, *Phys. Fluids*, *18*, 1045–1050, doi:10.1063/1.861253.

Dendy, R. O., C. N. Lashmore-Davies, K. G. McClements, and G. A. Cottrell (1994), The excitation of obliquely propagating fast Alfvén waves at fusion ion cyclotron harmonics, *Phys. Plasmas*, *1*, 1918–1928, doi:10.1063/1.870647.

Denton, R. E., M. K. Hudson, S. A. Fuselier, and B. J. Anderson (1993), Electromagnetic ion cyclotron waves in the plasma depletion layer, *J. Geophys. Res.*, *98*, 13,477–13,490, doi:10.1029/93JA00796.

Denton, R. E., M. J. Engebretson, A. Keiling, A. P. Walsh, S. P. Gary, P. M. E. DéCréAu, C. A. Cattell, and H. RèMe (2010), Multiple harmonic ULF waves in the plasma sheet boundary layer: Instability analysis, *J. Geophys. Res.*, *115*, A12224, doi:10.1029/2010JA015928.

Dimmock, A. P., A. Osmane, T. I. Pulkkinen, and K. Nykyri (2015), A statistical study of the dawn-dusk asymmetry of ion temperature anisotropy and mirror mode occurrence in the terrestrial dayside magnetosheath using THEMIS data, *J. Geophys. Res. Space Physics*, *120*, 5489–5503, doi:10.1002/2015JA021192.

Engebretson, M. J., et al. (2010), Multiple harmonic ULF waves in the plasma sheet boundary layer observed by Cluster, *J. Geophys. Res.*, *115*, A12225, doi:10.1029/2010JA015929.

Florinski, V., G. P. Zank, J. Heerikhuisen, Q. Hu, and I. Khazanov (2010), Stability of a pickup ion ring-beam population in the outer heliosheath: Implications for the IBEX ribbon, *Astrophys. J.*, *719*, 1097–1103, doi:10.1088/0004-637X/719/2/1097.

Florinski, V., J. Heerikhuisen, J. Niemiec, and A. Ernst (2016), The IBEX ribbon and the pickup ion ring stability in the outer heliosheath. I. Theory and hybrid simulations, *Astrophys. J.*, *826*, 197, doi:10.3847/0004-637X/826/2/197.

Fu, X., M. M. Cowee, V. K. Jordanova, S. P. Gary, G. D. Reeves, and D. Winske (2016), Predicting electromagnetic ion cyclotron wave amplitude from unstable ring current plasma conditions, *J. Geophys. Res. Space Physics*, *121*, 10,954–10,965, doi:10.1002/2016JA023303.

Gamayunov, K., M. Zhang, and H. Rassoul (2010), Pitch angle scattering in the outer heliosheath and formation of the interstellar boundary explorer ribbon, *Astrophys. J.*, *725*, 2251–2261, doi:10.1088/0004-637X/725/2/2251.

Gary, S. P. (1992), The mirror and ion cyclotron anisotropy instabilities, *J. Geophys. Res.*, *97*, 8519–8529, doi:10.1029/92JA00299.

Gary, S. P. (1993), *Theory of Space Plasma Microinstabilities*, 193 pp., Cambridge Univ. Press, Cambridge, U. K.

Gary, S. P., and M. A. Lee (1994), The ion cyclotron anisotropy instability and the inverse correlation between proton anisotropy and proton beta, *J. Geophys. Res.*, *99*(A6), 11,297–11,301, doi:10.1029/94JA00253.

Gary, S. P., and C. D. Madland (1988), Electromagnetic ion instabilities in a cometary environment, *J. Geophys. Res.*, *93*, 235–241, doi:10.1029/JA093iA01p00235.

Gary, S. P., D. W. Foosland, C. W. Smith, M. A. Lee, and M. L. Goldstein (1984), Electromagnetic ion beam instabilities, *Phys. Fluids*, *27*, 1852–1862, doi:10.1063/1.864797.

Gary, S. P., S. Hinata, C. D. Madland, and D. Winske (1986), The development of shell-like distributions from newborn cometary ions, *Geophys. Res. Lett.*, *13*, 1364–1367, doi:10.1029/GL013i013p01364.

Gary, S. P., M. F. Thomsen, L. Yin, and D. Winske (1995), Electromagnetic proton cyclotron instability: Interactions with magnetospheric protons, *J. Geophys. Res.*, *100*, 21,961–21,972, doi:10.1029/95JA01403.

Gary, S. P., R. M. Skoug, J. T. Steinberg, and C. W. Smith (2001), Proton temperature anisotropy constraint in the solar wind: ACE observations, *Geophys. Res. Lett.*, *28*, 2759–2762, doi:10.1029/2001GL013165.

Gary, S. P., K. Liu, D. Winske, and R. E. Denton (2010), Ion Bernstein instability in the terrestrial magnetosphere: Linear dispersion theory, *J. Geophys. Res.*, *115*, A12209, doi:10.1029/2010JA015965.

Gary, S. P., K. Liu, and L. Chen (2012), Alfvén-cyclotron instability with singly ionized helium: Linear theory, *J. Geophys. Res.*, *117*, A08201, doi:10.1029/2012JA017740.

Gary, S. P., X. Fu, M. M. Cowee, D. Winske, and K. Liu (2017), Scalings for the Alfvén-cyclotron instability: Linear dispersion theory and hybrid particle-in-cell simulations, *J. Geophys. Res. Space Physics*, *122*, 464–474, doi:10.1002/2016JA023425.

Gendrin, R. (1983), Wave particle interactions as an energy transfer mechanism between different particle species, *Space Sci. Rev.*, *34*, 271–287, doi:10.1007/BF00175283.

Gendrin, R., M. Ashour-Abdalla, Y. Omura, and K. Quest (1984), Linear analysis of ion cyclotron interaction in a multicomponent plasma, *J. Geophys. Res.*, *89*, 9119–9124, doi:10.1029/JA089iA10p09119.

Gulelmi, A. V., B. I. Klaine, and A. S. Potapov (1975), Excitation of magnetosonic waves with discrete spectrum in the equatorial vicinity of the plasmapause, *Planet. Space Sci.*, *23*, 279–286, doi:10.1016/0032-0633(75)90133-6.

Hasegawa, A. (1969), Drift mirror instability of the magnetosphere, *Phys. Fluids*, *12*, 2642–2650, doi:10.1063/1.1692407.

Heerikhuisen, J., N. V. Pogorelov, G. P. Zank, G. B. Crew, P. C. Frisch, H. O. Funsten, P. H. Janzen, D. J. McComas, D. B. Reisenfeld, and N. A. Schwadron (2010), Pick-up ions in the outer heliosheath: A possible mechanism for the interstellar boundary explorer ribbon, *Astrophys. J. Lett.*, *708*, L126–L130, doi:10.1088/2041-8205/708/2/L126.

Hellinger, P., P. Trávníček, J. C. Kasper, and A. J. Lazarus (2006), Solar wind proton temperature anisotropy: Linear theory and WIND/SWE observations, *Geophys. Res. Lett.*, *33*, L09101, doi:10.1029/2006GL025925.

Herčík, D., P. M. Trávníček, J. R. Johnson, E.-H. Kim, and P. Hellinger (2013), Mirror mode structures in the asymmetric Hermean magnetosheath: Hybrid simulations, *J. Geophys. Res. Space Physics*, *118*, 405–417, doi:10.1029/2012JA018083.

Hoilijoki, S., M. Palmroth, B. M. Walsh, Y. Pfau-Kempf, S. von Alfthan, U. Ganse, O. Hannuksela, and R. Vainio (2016), Mirror modes in the Earth's magnetosheath: Results from a global hybrid-Vlasov simulation, *J. Geophys. Res. Space Physics*, *121*, 4191–4204, doi:10.1002/2015JA022026.

Horne, R. B., G. V. Wheeler, and H. S. C. K. Alleyne (2000), Proton and electron heating by radially propagating fast magnetosonic waves, *J. Geophys. Res.*, *105*, 27,597–27,610, doi:10.1029/2000JA000018.

Kasper, J. C., A. J. Lazarus, S. P. Gary, and A. Szabo (2003), Solar wind temperature anisotropies, *Solar Wind Ten*, *679*, 538–541, doi:10.1063/1.1618653.
Kennel, C. (1966), Low-frequency whistler mode, *Phys. Fluids*, *9*, 2190–2202, doi:10.1063/1.1761588.
Kennel, C. F., and F. Engelmann (1966), Velocity space diffusion from weak plasma turbulence in a magnetic field, *Phys. Fluids*, *9*, 2377–2388, doi:10.1063/1.1761629.
Liu, K., D. S. Lemons, D. Winske, and S. P. Gary (2010), Relativistic electron scattering by electromagnetic ion cyclotron fluctuations: Test particle simulations, *J. Geophys. Res.*, *115*, A04204, doi:10.1029/2009JA014807.
Liu, K., E. Möbius, S. P. Gary, and D. Winske (2012), Pickup proton instabilities and scattering in the distant solar wind and the outer heliosheath: Hybrid simulations, *J. Geophys. Res.*, *117*, A10102, doi:10.1029/2012JA017969.
Ma, Q., W. Li, L. Chen, R. M. Thorne, and V. Angelopoulos (2014), Magnetosonic wave excitation by ion ring distributions in the Earth's inner magnetosphere, *J. Geophys. Res. Space Physics*, *119*, 844–852, doi:10.1002/2013JA019591.
McClements, K. G., R. O. Dendy, and C. N. Lashmore-Davis (1994), A model for the generation of obliquely propagating ULF waves near the magnetic equator, *J. Geophys. Res.*, *99*, 23,685–23,693, doi:10.1029/94JA01979.
McComas, D., et al. (2005), The Interstellar Boundary Explorer (IBEX) mission, in *Solar Wind 11/SOHO 16, Connecting Sun and Heliosphere*, vol. 592, edited by B. Fleck, T. H. Zurbuchen, and H. Lacoste, p. 689. [Available at http://ads.ari.uni-heidelberg.de/abs/2005ESASP.592..689M.]
McComas, D. J., et al. (2009a), IBEX—Interstellar Boundary Explorer, *Space Sci. Rev.*, *146*, 11–33, doi:10.1007/s11214-009-9499-4.
McComas, D. J., et al. (2009b), Global observations of the interstellar interaction from the Interstellar Boundary Explorer (IBEX), *Science*, *326*, 959–962, doi:10.1126/science.1180906.
McComas, D. J., H. O. Funsten, S. A. Fuselier, W. S. Lewis, E. Möbius, and N. A. Schwadron (2011), IBEX observations of heliospheric energetic neutral atoms: Current understanding and future directions, *Geophys. Res. Lett.*, *38*, L18101, doi:10.1029/2011GL048763.
McComas, D. J., W. S. Lewis, and N. A. Schwadron (2014), IBEX's Enigmatic Ribbon in the sky and its many possible sources, *Rev. Geophys.*, *52*, 118–155, doi:10.1002/2013RG000438.
McKean, M. E., D. Winske, and S. P. Gary (1992), Mirror and ion cyclotron anisotropy instabilities in the magnetosheath, *J. Geophys. Res.*, *97*, 19,421–19,432, doi:10.1029/92JA01842.
Meredith, N. P., R. B. Horne, and R. R. Anderson (2008), Survey of magnetosonic waves and proton ring distributions in the Earth's inner magnetosphere, *J. Geophys. Res.*, *113*, A06213, doi:10.1029/2007JA012975.
Min, K., and K. Liu (2015), Fast magnetosonic waves driven by shell velocity distributions, *J. Geophys. Res. Space Physics*, *120*, 2739–2753, doi:10.1002/2015JA021041.
Min, K., and K. Liu (2016a), Proton velocity ring-driven instabilities in the inner magnetosphere: Linear theory and particle-in-cell simulations, *J. Geophys. Res. Space Physics*, *121*, 475–491, doi:10.1002/2015JA022042.
Min, K., and K. Liu (2016b), Understanding the growth rate patterns of ion Bernstein instabilities driven by ring-like proton velocity distributions, *J. Geophys. Res. Space Physics*, *121*, 3036–3049, doi:10.1002/2016JA022524.
Min, K., and K. Liu (2016c), Ion Bernstein instability dependence on the proton-to-electron mass ratio: Linear dispersion theory, *J. Geophys. Res. Space Physics*, *121*, 6692–6710, doi:10.1002/2016JA022850.
Min, K., K. Liu, and S. P. Gary (2016), Scalings of Alfvén-cyclotron and ion Bernstein instabilities on temperature anisotropy of a ring-like velocity distribution in the inner magnetosphere, *J. Geophys. Res. Space Physics*, *121*, 2185–2193, doi:10.1002/2015JA022134.
Möbius, E., K. Liu, H. Funsten, S. P. Gary, and D. Winske (2013), Analytic model of the IBEX Ribbon with neutral solar wind based ion pickup beyond the heliopause, *Astrophys. J.*, *766*, 129, doi:10.1088/0004-637X/766/2/129.
Niemiec, J., V. Florinski, J. Heerikhuisen, and K.-I. Nishikawa (2016), The IBEX ribbon and the pickup ion ring stability in the outer heliosheath: II. Monte-Carlo and particle-in-cell model results, *Astrophys. J.*, *826*, 198, doi:10.3847/0004-637X/826/2/198.
Perraut, S., A. Roux, P. Robert, R. Gendrin, J.-A. Sauvaud, J.-M. Bosqued, G. Kremser, and A. Korth (1982), A systematic study of ULF waves above f_{H+} from GEOS 1 and 2 measurements and their relationships with proton ring distributions, *J. Geophys. Res.*, *87*(A8), 6219–6236, doi:10.1029/JA087iA08p06219.
Porazik, P., and J. R. Johnson (2013), Gyrokinetic particle simulation of nonlinear evolution of mirror instability, *J. Geophys. Res. Space Physics*, *118*, 7211–7218, doi:10.1002/2013JA019308.
Riquelme, M. A., E. Quataert, and D. Verscharen (2015), Particle-in-cell simulations of continuously driven mirror and ion cyclotron instabilities in high beta astrophysical and heliospheric plasmas, *Astrophys. J.*, *800*, 27, doi:10.1088/0004-637X/800/1/27.
Russell, C. T., R. E. Holzer, and E. J. Smith (1970), OGO 3 observations of ELF noise in the magnetosphere: 2. The nature of the equatorial noise, *J. Geophys. Res.*, *75*(4), 755–768, doi:10.1029/JA075i004p00755.
Russell, C. T., W. Riedler, K. Schwingenschuh, and Y. Yeroshenko (1987), Mirror instability in the magnetosphere of Comet Halley, *Geophys. Res. Lett.*, *14*, 644–647, doi:10.1029/GL014i006p00644.
Santolík, O., J. S. Pickett, D. A. Gurnett, M. Maksimovic, and N. Cornilleau-Wehrlin (2002), Spatiotemporal variability and propagation of equatorial noise observed by Cluster, *J. Geophys. Res.*, *107*(A12), 1495, doi:10.1029/2001JA009159.
Schwadron, N. A., et al. (2009), Comparison of interstellar boundary explorer observations with 3D global heliospheric models, *Science*, *326*, 966–968, doi:10.1126/science.1180986.
Shoji, M., Y. Omura, B. T. Tsurutani, O. P. Verkhoglyadova, and B. Lembege (2009), Mirror instability and L-mode electromagnetic ion cyclotron instability: Competition in the Earth's magnetosheath, *J. Geophys. Res.*, *114*, A10203, doi:10.1029/2008JA014038.
Shoji, M., Y. Omura, and L.-C. Lee (2012), Multidimensional nonlinear mirror-mode structures in the Earth's magnetosheath, *J. Geophys. Res.*, *117*, A08208, doi:10.1029/2011JA017420.
Stix, T. H. (1992), *Waves in Plasmas*, Am. Inst. of Phys., New York.
Sulem, P.-L. (2011), Nonlinear mirror modes in space plasmas, in *American Institute of Physics Conference Series*, vol. 1356, edited by I. Zhelyazkov and T. Mishonov, pp. 159–176, doi:10.1063/1.3598103. [Available at http://ads.ari.uni-heidelberg.de/abs/2011AIPC.1356..159S.]
Summerlin, E. J., A. F. Viñas, T. E. Moore, E. R. Christian, and J. F. Cooper (2014), On the stability of pick-up ion ring distributions in the outer heliosheath, *Astrophys. J.*, *793*, 93, doi:10.1088/0004-637X/793/2/93.
Tsurutani, B. T., D. J. Southwood, E. J. Smith, and A. Balogh (1992), Nonlinear magnetosonic waves and mirror mode structures in the March 1991 ULYSSES interplanetary event, *Geophys. Res. Lett.*, *19*, 1267–1270, doi:10.1029/92GL00782.
Tsurutani, B. T., G. S. Lakhina, E. J. Smith, B. Buti, S. L. Moses, F. V. Coroniti, A. L. Brinca, J. A. Slavin, and R. D. Zwickl (1999), Mirror mode structures and ELF plasma waves in the Giacobini-Zinner magnetosheath, *Nonlinear Processes Geophys.*, *6*, 229–234.
Vandas, M., and P. Hellinger (2015), Linear dispersion properties of ring velocity distribution functions, *Phys. Plasmas*, *22*(6), 62107, doi:10.1063/1.4922073.

Volwerk, M., T. L. Zhang, M. Delva, Z. Vörös, W. Baumjohann, and K.-H. Glassmeier (2008), First identification of mirror mode waves in Venus' magnetosheath?, *Geophys. Res. Lett.*, *35*, L12204, doi:10.1029/2008GL033621.

Walker, S. N., A. G. Demekhov, S. A. Boardsen, N. Y. Ganushkina, D. G. Sibeck, and M. A. Balikhin (2016), Cluster observations of non-time continuous magnetosonic waves, *J. Geophys. Res. Space Physics*, *121*, 9701–9716, doi:10.1002/2016JA023287.

Winske, D., and K. B. Quest (1986), Electromagnetic ion beam instabilities—Comparison of oneand two-dimensional simulations, *J. Geophys. Res.*, *91*, 8789–8797, doi:10.1029/JA091iA08p08789.

Winske, D., C. S. Wu, Y. Y. Li, Z. Z. Mou, and S. Y. Guo (1985), Coupling of newborn ions to the solar wind by electromagnetic instabilities and their interaction with the bow shock, *J. Geophys. Res.*, *90*, 2713–2726, doi:10.1029/JA090iA03p02713.

Wu, C. S., and R. C. Davidson (1972), Electromagnetic instabilities produced by neutral-particle ionization in interplanetary space, *J. Geophys. Res.*, *77*, 5399–5406, doi:10.1029/JA077i028p05399.

Wu, C. S., and R. E. Hartle (1974), Further remarks on plasma instabilities produced by ions born in the solar wind, *J. Geophys. Res.*, *79*, 283–285, doi:10.1029/JA079i001p00283.

Wu, C. S., J. D. Gaffey Jr., and D. Winske (1986), Rapid pickup of cometary ions due to strong magnetic turbulence, *Geophys. Res. Lett.*, *13*, 865–868, doi:10.1029/GL013i008p00865.

Wu, C. S., D. Krauss-Varban, and T. S. Huo (1988), A mirror instability associated with newly created ions in a moving plasma, *J. Geophys. Res.*, *93*, 11,527–11,532, doi:10.1029/JA093iA10p11527.

Xiao, F., Q. Zhou, Z. He, C. Yang, Y. He, and L. Tang (2013), Magnetosonic wave instability by proton ring distributions: Simultaneous data and modeling, *J. Geophys. Res. Space Physics*, *118*, 4053–4058, doi:10.1002/jgra.50401.

Yoon, P. H. (1992), Further evolution of velocity shell distribution of cometary and interstellar pickup ions and excitation of oblique Alfven waves, *J. Geophys. Res.*, *97*, 6467–6477, doi:10.1029/92JA00137.

Yoon, P. H., and J. Seough (2012), Quasilinear theory of anisotropy-beta relation for combined mirror and proton cyclotron instabilities, *J. Geophys. Res.*, *117*, A08102, doi:10.1029/2012JA017697.

Zank, G. P. (1999), Interaction of the solar wind with the local interstellar medium: A theoretical perspective, *Space Sci. Rev.*, *89*, 413–688, doi:10.1023/A:1005155601277.